ITSC 2015—Proceedings of the International Thermal Spray Conference
May 11–14, 2015, Long Beach, California, USA
A. McDonald, A. Agarwal, G. Bolelli, A. Concustell, Y.-C. Lau, F.-L. Toma, E. Turunen, C. Widener, editors

Self-Healing Plasma Sprayed Ceramic Coatings

Z. Ilhan, A. Hornes, N. Sata, O. Freitag, A. Ansar, G. Schiller, A. Friedrich
German Aerospace Centre (DLR), Stuttgart, Germany

V. Guski, U. Weber, A. Krebs, S. Schmauder
Institute for Materials Testing, Materials Science and Strength of Materials (IMWF), University of Stuttgart, Stuttgart, Germany

Abstract

The current paper reports self-healing plasma sprayed Mg-spinel ($MgAl_2O_4$) coatings. The coatings were used for electrical insulation in high temperature fuel cells. A range of potential self-healing additives consisting of SiC+X (where X was BaO, CaO, ZnO, Y_2O_3, GeO_2, Ta_2O_5, V_2O_5) were characterized and SiC+Y_2O_3 was initially selected for coating development. Coatings of spinel with 20wt% additive were developed using vacuum plasma spraying (VPS) or atmospheric plasma spraying (APS). In the developed coatings, self-healing was demonstrated after heat treatment at 1050°C in air for 10 hour. Thermophysical and thermomechanical properties of self-healing coatings were determined and compared to spinel coatings. Lastly, a modelling technique is presented to simulate the effective elastic moduli of the coatings. Numerical results based on microstructural simulations showed good agreement with experimental data.

Introduction

Catastrophic failure in ceramics is a major limiting factor constraining their use in many applications. It has been mostly addressed by introducing a toughening mechanism such as reinforcement with fibers, whiskers, ductile or brittle particles, or phase transformation. An alternative approach consists of incorporating crack healing capabilities, which offer improved reliability and service time of ceramic components. Though reported already in 1970's [1, 2], this approach has limited work attributed to it to this day. Most studied self-healing ceramics are oxide ceramic matrix composites (CMCs) having 15 to 20 wt% of well distributed SiC particles such as Al_2O_3/SiC [3, 4] and mullite/SiC [5, 6]. It was established that in SiC containing ceramic composites the healing occurs due to oxidation reaction, associated with volume expansion of new phases into the defects [7]:

$$SiC + 2O_2 \rightarrow SiO_2+CO_2\ (CO) \quad (1)$$

Other studies suggested healing can be improved by promoting vitreous phase formation by using SiC+Y_2O_3 [8]:

$$2SiC + Y_2O_3 + 4O_2 \rightarrow Y_2Si_2O_7+2CO_2\ (CO) \quad (2)$$

As a result, cracks up to 100 µm were fully healed and the bending strength was increased by several folds.
Self-healing was also developed in other systems including ZrO_2/SiC by thermal decomposition transformation to $ZrSiO_4$ and carbon black mixture [9]. Additionally, crack healing ability was investigated in non-oxide ceramics such as Si_3N_4 by introducing SiC [10,11]. In all materials presence of oxidizing environment is mandatory for a healing mechanism to occur and in most cases the minimum temperature at which full crack healing takes place has been reported at above 1000°C [3-11].

In high temperature fuel cells, appearance of defects in the sealing has been reported as the foremost cause of failure in fuel cell stacks [12,13]. The sealing, traditionally made of glass or glass-ceramic composites, guarantees flow of fuel gas and air in designated compartments. A leakage across the seal leads to catastrophic loss in cell potential and power output. Glass-based seals lack the necessary reliability especially when the cells have to undergo intermittent operation. In our earlier work [14], an alternative approach was proposed in which Ag-based filler material is used for sealing of two consecutive cells. As the filler alloy is electronically conductive, short circuiting between the cells is avoided by introducing an Mg-spinel coating in between. The electrically insulating spinel deposit is produced by plasma spraying. The schematic of sealing the approach is given in Fig. 1. In spite of enhanced reliability compared to glass-based seals, the coating +Ag-braze based seals suffer from defects and cracks in the coating. These defects, associated to the manufacturing process or arise due to thermal cycling, give site for further crack nucleation and propagation, decrease the elastic modulus, yield strength and fracture energy of the coatings.

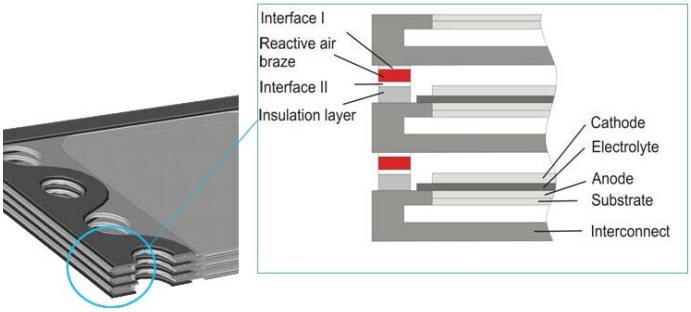

Figure 1: Schematic of the SOFC stack sealing based on active braze and insolating ceramic coating.

At elevated temperatures crack initiation and propagation mechanism changes and failure may occur at the featureless zones, as suggested by Lowrie and Rawlings [15]. Overall, the increase in temperature from room temperature to 800°C caused a 23–30% reduction in flexural strength of bulk 8YSZ. Ansar et al [16] have reported that the elastic modulus of plasma sprayed 8YSZ reduces from 35±2 GPa at room temperature (instead of 120 GPa for bulk material) to 16±1 GPa at 800°C. The decrease in elastic properties of such a coating was almost twice to bulk material and this was associated to the intrinsic elastic modulus of the YSZ but also to the structure of the splat boundaries.

Incorporation of a material that can heal these defects at elevated temperature can significantly improve the stress bearing capability and fracture strength of these coatings. The potential of such an approach is investigated in this paper. Insulating spinel coatings are primarily exposed to oxidizing environment which makes it realistic to achieve a crack healing mechanism. Although, a range of potential self-healing additives consisting of SiC+X (where X was BaO, CaO, ZnO, Y_2O_3, GeO_2, Ta_2O_5, V_2O_5) were tested, this paper reports results with SiC+Y_2O_3.

Experimental Procedure

Feedstock Materials

Table 1 lists different feedstock powders used in this work along with their particle size. All powders were on a 99.5% or better purity level. Spinel was fused and crushed angular powder whereas the pre-synthesized self-healing powder was an alloyed-fused angular powder. Both powders were suitable for thermal spraying.

Table 1: List of feedstock powders

Powder	Source	Particle size
$MgAl_2O_4$	Oerlikon Metco (CH)	-50+5 µm
SiC	Iolitec (D)	d50= 1.2 µm
Nano-SiC	Iolitec (D)	d50= 50-60 nm
Y_2O_3	Iolitec (D)	d50= 1.2 µm
Nano-Y_2O_3	Iolitec (D)	d50=30-50 nm
Alloyed $MgAl_2O_4$+ 20 wt% (SiC+Y_2O_3)	Saan Innovation (S)	-60+5 µm

Plasma Spraying

$MgAl_2O_4$ and $MgAl_2O_4$ with SiC+Y_2O_3 were sprayed either using vacuum plasma spraying (VPS) with an F4 torch having a delaval Mach 3 6 mm diameter anode nozzle or atmospheric plasma spraying (APS) with a Triplex Pro 210 gun (Oerlikon Metco, CH) with a 9 mm anode. The process optimization was done using partial factorial design of experiment in which inputs were: arc current and flow rates of plasma gases Ar, He and H_2. The outputs used for process optimization are listed in Table 2 along with their acceptable and attained values after optimization[1]. 50±4 µm thick coatings were produced on porous metallic Fe-Cr substrates from Plansee (A). These samples were used to measure air leak through coating which determined the open porosity in it as low leakage indicated lower open porosity and was desirable. The method is explained elsewhere [17]. In addition, free-standing 1 mm thick coatings were prepared for dilatometry and flexural test. For this purpose, coatings were sprayed on 7 mm x 44 mm plain carbon steel substrates followed by substrate dissolution by acid treatment in dilute sulfuric acid solution (1N) and applying dc voltage between the substrate and a counter metal electrode of 1.0-1.1 V. For conductivity and structural analysis 70±6 µm thick coatings were sprayed on Fe-Cr steel (Crofer 22APU) from Thyssen VDI (D).

Table 2: Outputs used for optimization of plasma spray process for self-healing coatings after partial factorial DoE

Plasma Spray Process Optimization Outputs	Desired value	Attained value	
		VPS	APS
Leak rate (Pa.m/s)	< 7	4.2±0.4	5.7±0.9
Deposition efficiency (%)	>55	52±1	67±1
In-flight reaction of self-healing additives (%)	<10	*	°
Interconnect bending (mm)	<1.5	1.2±0.3	0.8 ±0.1

* the criterion was of no relevance in VPS
° reacted phase detected but it was too low to be quantified reliably

Characterization

SiC with Y_2O_3 was mixed using laboratory mortar and pestle and tested in a Pt crucible using a thermo gravitation analyzer (TGA) with a parallel running differential scanning calorimetry (DSC) using STA 449C Jupiter® from Netzsch (D). 30 ml/min of Argon 5.0 was used as protection gas and the reaction gas was 30 ml/min synthetic air (80% N_2 and 20% O_2). The samples were heated up to 1200°C with a heating rate of 5 K/min and then cooled down under atmospheric conditions. After cooling the reacted samples were analyzed using X-ray diffractometry (XRD), Raman spectroscopy and X-ray photoelectron spectroscopy (XPS). Diffractograms were recorded with a D8 Discover GADDS, equipped with a VÅNTEC-2000 area detector. Exposures were made in reflection mode with a tuned monochromatic and parallel X-ray beam (Cu-Kα). Raman spectroscopy was conducted with a confocal Raman microscope (LabRam 800, Horiba Jobin Ybon). The green laser line of an argon ion laser (wavelength = 514.5 nm) was used for excitation. XPS

[1] Detailed statistical and regression analysis will be submitted in a separate paper.

analyses were carried out with a Thermo ESCALAB 250 (Thermo Electron Corporation, East Grinstead West Sussex, UK). In these tests ultra-high vacuum conditions were employed with a base pressure of 1×10^{-9} mbar. Non-monochromated Al Kα radiation at 1486 eV was used. Operation at 300 W in combination with a hemispherical six-channeltron electron analyzer operated in a large area mode (analyzed surface area = 50 mm^2) was used. The binding energies were referenced to the C1s peak of the C-H species at 285.0 eV. Si2p deconvolution was made using the curve fitting of the Advantage software. The microscopy was done on ZEISS a UltraPlus scanning electron microscope (ZEISS, Germany). Dilatometry was done on free standing 1 mm thick coatings. All samples were tested in air up to 1000 °C and two runs were recorded each time. For conductivity measurements, 70±6 µm thick coatings on 50x50 mm² Crofer 22 APU were air brazed with counter plate of 50x50 mm² Crofer 22 APU. The procedure is explained elsewhere [14]. Four probe dc measurements were conducted as function of temperature. Elastic properties of the free-standing coating were determined by 4-point bending test for $MgAl_2O_4$. The investigated samples had a size of 0.8 x 3.8 x 47 mm. The loading velocity was kept on 0.5 mm/min. The measured force-displacement curves deliver the basis for an inverse modelling procedure. This method provides the Young's modulus iteratively by successive feeding back results to adjust input parameters to increase accuracy. The simulated force-displacement curve is compared with the measured curve repeatedly until the effective elastic modulus of the ceramic with the best match is derived. Using this methodology, an effective elastic modulus of 90 GPa for the free-standing ceramic was determined.

Results and Discussion

Characterization of Self-Healing Additive

TGA / DSC data for nano and micro sized SiC are shown in Fig. 2 (a). For nano-SiC a broad depression in the DSC curve till 900 °C can be due to adsorption of oxygen on the surface. This was also observed earlier for nano-SiC by [18] and for highly porous carbon materials by [19]. In nano-SiC, the adsorption was associated with approximately 1% increase in the mass while heating the sample up to 900 °C. For the micro-sized SiC powder, owning to lower specific surface area, this effect was not observed. To validate this hypothesis, TGA/DSC of nano-SiC was also carried out in Ar and it is plotted in Fig. 2 (a). As it can be noticed, the DSC and TGA curves appeared flat within the scale resolution, supporting the hypothesis. Regardless of the particle size of SiC, an exothermic reaction above 900°C when heated in air and an increase in its weight can be attributed to its oxidation. For the mixture of nano-SiC+nano-Y_2O_3 with a 2:1 molar ratio (Fig 2 (b)), a decrease in the mass up to 600°C was observed followed by an increase above 900°C. The latter can be again attributed to oxidation of SiC, whereas the initial loss may be due to the evaporation of adsorbed water molecules from the Y_2O_3 surface, as previously reported by [20]. XRD pattern of the powder mixture after the TGA analysis (Fig. 3) revealed Y_2SiO_5 formation. As $Y_2Si_2O_7$ may also form, being a glassy phase, it could not be detected by XRD.

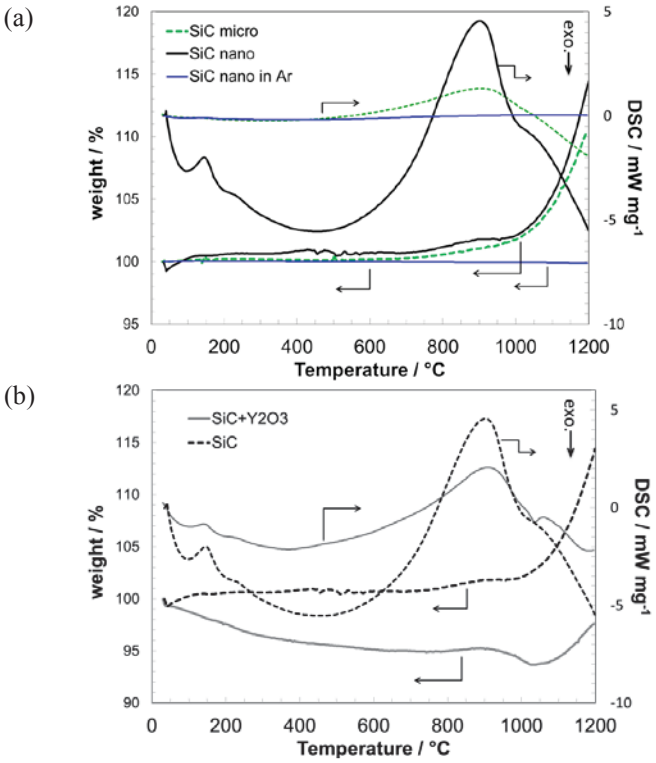

Figure 2: (a) TGA/DSC data of nano-SiC treated in air or Ar and of micro-SiC treated in Air (b) TGA/DSC data of nano-SiC (dotted lines) and nano-SiC+nanoY2O3 (solid lines).

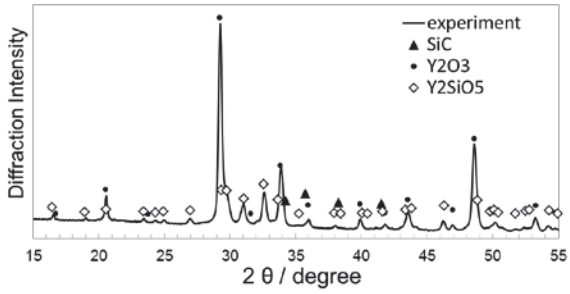

Figure 3: XRD pattern (zeroed base line) of nano-SiC+nano-Y_2O_3 mixture after TGA analysis. The solid dot solid triangle and open triangle denote Y_2O_3, SiC and Y_2SiO_5 phases

Figure 4 (a) shows the XPS Si2p region of a SiC raw sample. The main peak at 100.5 eV is assigned to silicon carbide while the other contributions at higher binding energy are attributed to silicon oxides with different oxidation state Si^{2+} (102.2 eV) [21] and Si^{4+} (103.5 eV) [22]. Figure 4 (b) displays the different behavior detected for pure SiC and mixed samples (SiC+Y_2O_3) after annealing. Two main contributions are detected in each spectrum. For pure SiC specimen, contributions at 100.2 eV and 101.8 eV associated with SiC and a silicon oxide with lower oxidation state (<2) [21], respectively. Nevertheless, one contribution at higher binding energy (ca. 102.4 eV), accompanied by another at lower energies centered at 100.4 eV, appeared for the composites. The latter is associated with Si-C species as before while the former would indicate the formation of a metal silicate [23]. Relative amount of this species decreases as annealing time is

increased, which could be related to a migration into the bulk of the material.

The interaction between SiC and Y_2O_3 was further investigated by the microscopic Raman spectroscopy of samples treated at 1050°C. In Fig. 5, Raman spectra of SiC and mixture are given. The Raman peaks in the graph are all stretching modes of the C-C bonds [24]. Such C-C vibrations are of amorphous or graphite carbons on the surface, which can be present in nano-SiC used in this work. Such findings were also reported earlier for nano-SiC [25]. The difference in the TGA results of micro- and nano-SiC might also come from the difference of the surface. It was observed for SiC powder that these modes change in their intensity and the peak widths as well as Raman shifts; the contribution of SiC phase, however, remains even after annealing for 10 hours at 1050°C. On the contrary, the stretching modes of the C-C bonds disappeared when the SiC-Y_2O_3 powder mixture is annealed already for 1 hour at this temperature. This suggests that higher kinetics of the healing reaction can be attained in the case of the mixture and healing time can be as short as 1 hour.

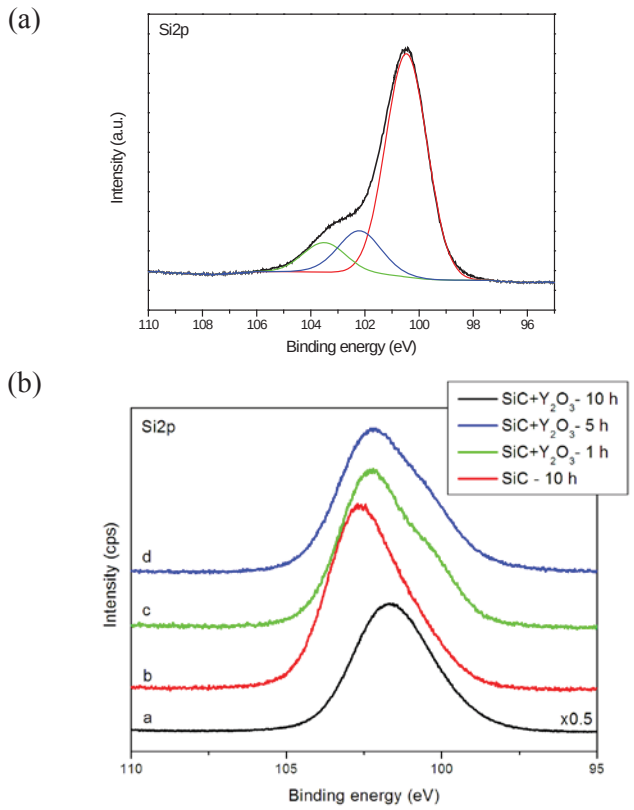

Figure 4: (a) XPS Si2p region data of feedstock SiC, and (b) SiC and SiC+Y_2O_3 after annealing in air at 1050°C.

Self-Healing Plasma Sprayed Coatings

Figure 6 illustrates the structure of self-healing air plasma sprayed coating. The gray matrix is spinel, whereas the bright splats are of additive material, i.e SiC+Y_2O_3. In higher magnification micrograph of a splat of additive (Fig. 6 (b)), it can be observed that the dark particle of SiC are embedded in the brighter Y_2O_3. The self-healing coatings were fractured and heat treated at 1050°C in air for 1, 5 and 10 hours. As it can be seen from the micrographs of the as-sprayed fractured coating and the ones heat treated for one hour in Figs. 7 (a) and (b), crack healing was observed after 1 hour. However limited numbers of cracks with median length of less than 1 µm were healed. This can also be attributed to a "thermal healing". Hence, despite indication from the SiC+Y_2O_3 data from last section that a reactive phase formation may already occur after one hour, it was not conclusive when tested in a plasma sprayed coating for 1 or 5 hours. On the other hand, reactive vitreous phase formation was evident after 10hours of heat treatment and larger defects could be healed (Figs. 8 (a) and (b)). Within a matrix of parent ceramic, it can be expected that the additive material would have access to lower concentration of oxygen and slower transformation kinetics.

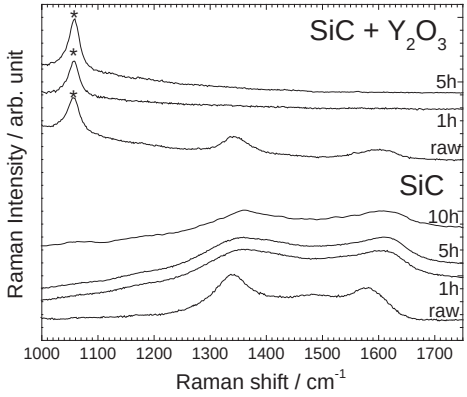

*Figure 5: Raman spectra of SiC and SiC+Y_2O_3 annealed at 1050°C in air. Peak marked as * is a luminescence from Y_2O_3.*

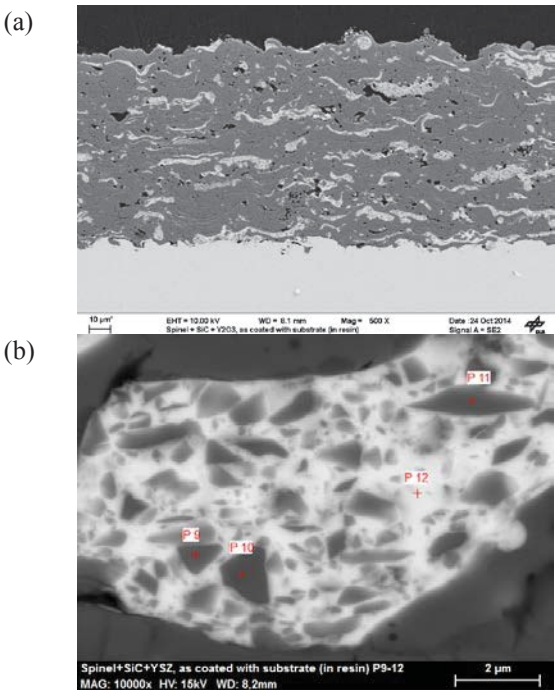

Figure 6: (a) SEM of air plasma sprayed self-healing coating. Bright additive particles are distributed in dark spinel matrix. (b) Higher magnification micrograph of a splat of additive material. Dark embedded particles are SiC and bright zone is Y_2O_3.

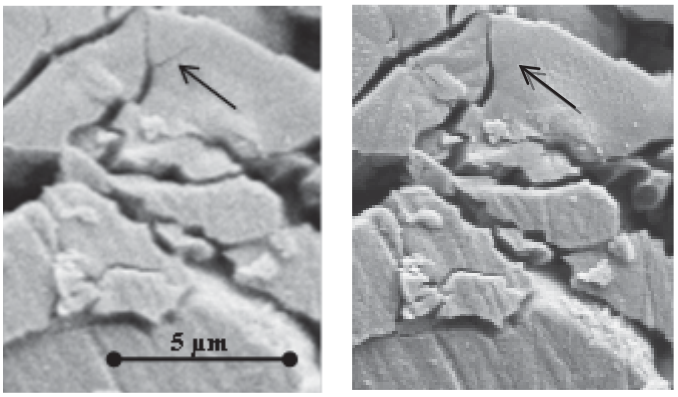

(a) (b)

Figure 7: (a) SEM micrographs of self-healing ceramic coating of in as-sprayed condition, and (b) heat treated at 1050°C for 1 hour in air. Arrow indicates the crack zone.

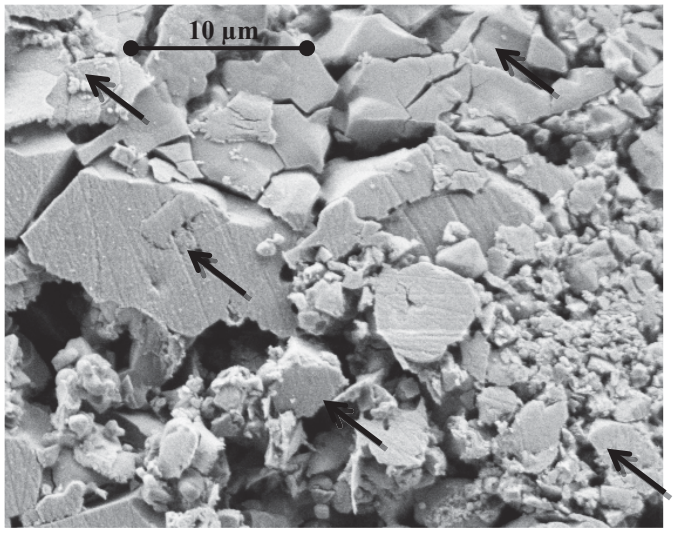

(a)

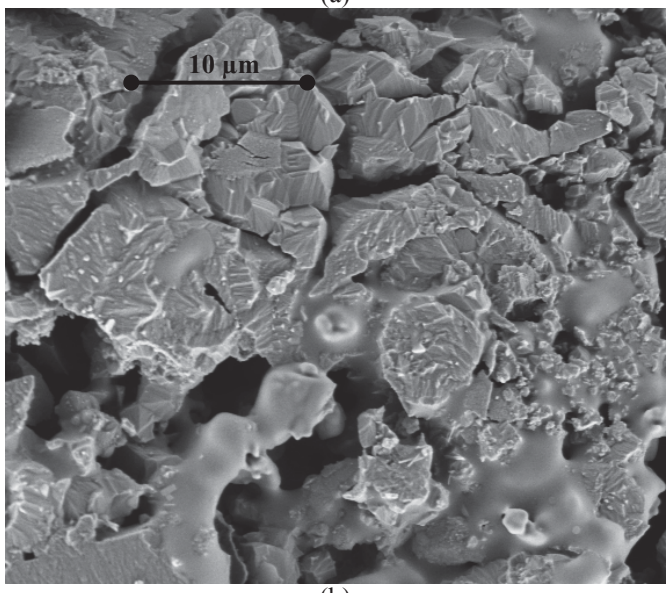

(b)

Figure 8: (a) Micrographs of fractured self-healing ceramic coating in as-sprayed condition, and (b) heat treated at 1050°C for 10 hour in air. Arrows indicate some of the zones with reactive vitreous phase formation and healing of defects.

The resistance data of pure spinel and spinel + 20wt% ($SiC+Y_2O_3$) coatings as a function of temperature is given in Fig. 8, revealing that the self-healing additive did not deteriorate the insulating properties of the coatings. The coefficient of thermal expansion (CTE) data, as summarized in Table 3, established that CTE of the spinel coating decreased as a function of SiC content which can be explained by the lower CTE of SiC. In the presence of composite additive ($SiC+Y_2O_3$), the CTE values were in between that of pure spinel and spinel+20wt%SiC which can be owing to the comparable CTE of Y_2O_3 to that of spinel. The coating, heat treated at 1050°C in air for 10 hours, had a comparable CTE to as-sprayed counterpart.

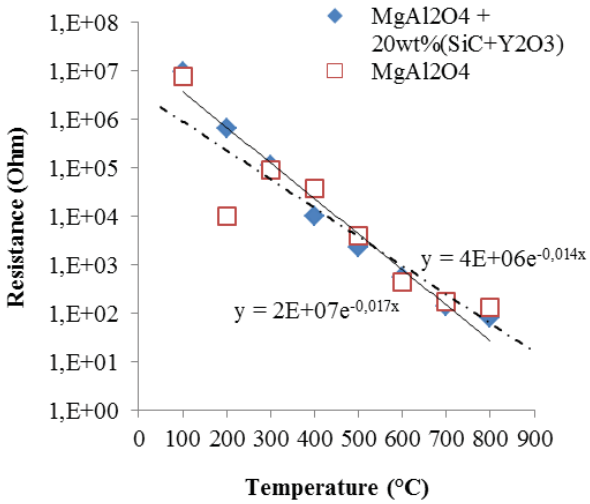

Figure 9: Electrical resistance values for $MgAl_2O_4$ and $MgAl_2O_4$+20wt% ($SiC+Y_2O_3$) coatings.

Table 3: CTE values of spinel and spinel+additive coatings

Coating Material	Technical α (10^{-6} /K^{-1})	
	At 800°C	At 850°C
$MgAl_2O_4$	8.31	8.39
$MgAl_2O_4$+ 5wt%SiC	8.07	8.15
$MgAl_2O_4$+ 20wt%SiC	7.94	8.01
$MgAl_2O_4$+ 20wt%($SiC+Y_2O_3$) As-sprayed	8.08	8.16
$MgAl_2O_4$+ 20wt%($SiC+Y_2O_3$) After heat treatment	8.06	8.13

Modelling and Simulation

An image-based approach [26,27,28] was employed to numerically determine the mechanical properties of two developed plasma-sprayed ceramic coatings namely $MgAl_2O_4$ and $MgAl_2O_4$ mixed with $SiC+Y_2O_3$. Numerical tensile tests were performed to determine the effective elastic modulus E_{eff}. The microstructure influences strongly this modulus. Finally, the numerical results are validated with the 4-point bending test results.

Microstructural Simulation—SEM Image-Based Modelling

The used microstructural approach provided relevant mechanical properties of the plasma-sprayed coating taking into account the characteristic microstructure such as pores or cracks [29]. Figure 10 shows the SEM images used to treat fine cracks, pores as well as the $SiC+Y_2O_3$ phase in the microstructural simulation. The SEM image magnification was 1000 x and micrographs sizes were 1024 x 768 pixels in treated images corresponding to a pixel resolution of 0.11 µm/px. At first, the grayscale $MgAl_2O_4$ SEM image (Fig. 10 (a)) was converted to a binary image using GIMP 2.6 [30] by applying a subsequent brightness threshold technique. A threshold value, which controls the grey values and describes the amount of pores, was selected by doing a parameter study with different brightness thresholds between 120 and 140. The procedure from the SEM image to the finite-element (FE) model is illustrated in Fig. 11. The image-based modelling can be divided into two steps. In the first step the SEM image is converted to a binary image with an adequate brightness threshold (Figs. 11 (a) and (b)). The effective elastic modulus is determined by means of numerical tensile tests in the second step (Figs. 11 (b) and (c)). Three cut-outs from the SEM image from Fig. 10 (a) representing a size of 50 µm x 50 µm were investigated (Fig. 12) obtaining an averaged effective modulus. The resulting effective elastic modulus of each threshold is compared with 4-point-bending test results afterwards.

To obtain the mechanical properties of the $MgAl_2O_4$ coating with $SiC+Y_2O_3$, the microstructure features were separated with a second threshold. The self-healing phase, as shown in Fig. 6 (b), was assumed as a homogenous phase. This homogenized Young's modulus of the interpenetrating phases of SiC and Y_2O_3 is calculated with the so called self-consistent matricity model (SCMM) developed at IMWF [31,32]. The input material parameters of the self-healing phase were calculated with this matricity model for the simulation. Young's modulus of SiC and Y_2O_3 were taken from literature [33]. The matricity model can provide the mechanical behavior of an isotropic two-phase composite with a coarse interpenetrating microstructure. This numerical description considers randomly distributed inclusions in a homogenous matrix and relies on an additional parameter of the microstructure, the so-called "Matricity (M)" of each phase with interpenetrating microstructures [28]. The matricity model was used to determine the Young's modulus and Poisson's ratio of the self-healing phase which contains 50% SiC and 50% Y_2O_3. The calculated Young's modulus of 267 GPa is used as input value for the $SiC+Y_2O_3$ phase in the numerical modelling. A cut-out with a size of 50 µm x 50 µm of the SEM image in Fig. 10 (b) is converted to a tri-color coded image (Fig. 13). With this tri-colored image and additionally the Young's modulus for the self-healing phase, the numerical tensile tests are then repeated.

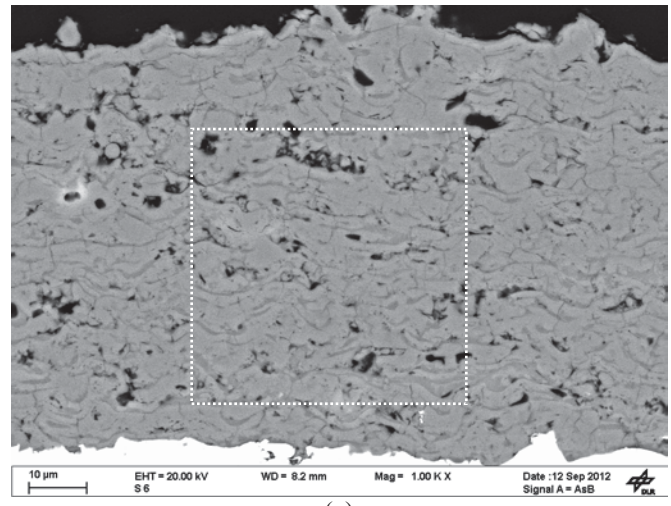

Figure 10: SEM image of the coatings, with pores and cracks (black), of (a) $MgAl_2O_4$ and (b) $MgAl_2O_4$ with $SiC+Y_2O_3$ with the investigated middle section (dashed box) used in Fig. 13(b)

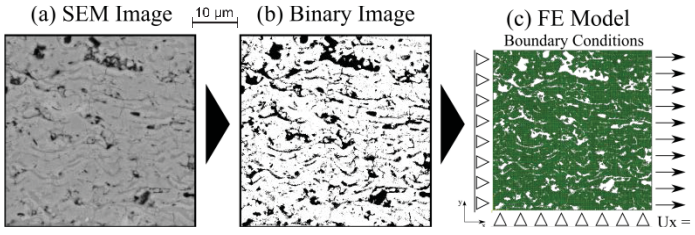

Figure 11: Schematic illustration of the image-based modelling procedure with the middle section, as exemplary

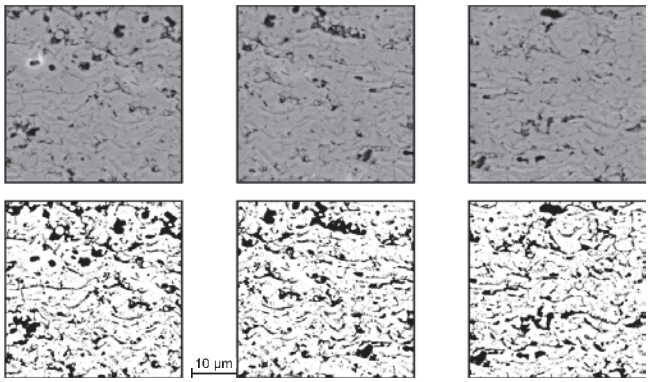

Figure 12: Three cut-outs (50 µm x 50 µm) in the SEM image (top) and the obtained binary image (bottom) with a threshold of 140 ((a) left section, (b) middle section, (c) right section)

Plasma spray process leads to a complex microstructure with an anisotropic effective modulus. Layered arrangements of fast-solidified ceramic droplets, so called splats cover the substrate stepwise with quite a dense layer including remaining porosities. Investigations have shown that the effective elastic modulus which is the Young's modulus influenced by microstructure features such as pores or cracks, in the spraying direction is smaller than the one perpendicular to the spraying direction [34]. In a plane oriented perpendicular to the spraying direction the effective modulus is isotropic. This type of anisotropic behavior (is also known as transversal isotropy and can be explained on the one hand by the round shape of splats, which are the solidified molten ceramic particles on the substrate surface and on the other hand by the interlamellar pores as well as the intralamellar cracks in the droplets of the material, respectively. Due to the transversal isotropic properties of plasma sprayed coatings, it is reasonable to consider the loading direction of the bending test for comparing the effective moduli. The object-oriented FE program OOF2, is used to transfer the binary images into a two dimensional FE mesh applied in ABAQUS FE program. OOF2 was developed by the National Institute of Standard and Technology, US [35]. With these FE models numerical tensile tests were performed with the FE solver ABAQUS. This study used plane strain elements (CPE [36]). The Mg-spinel bulk material of 210 GPa serves as input data for simulations [37].

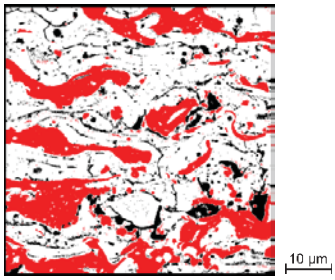

Figure 13: Color-separated image (50 µm x 50 µm) of the SEM-section with self-healing phase (white: $MgAl_2O_4$, red: self-healing phase, black: pores and cracks)

Boundary Conditions of the Numerical Tensile Tests

In numerical calculations the boundary conditions prove to influence the simulation results sensitively. Commonly, for microstructural simulations free, homogenous or periodic boundary conditions are reasonable. The choice of correct boundary conditions is crucial for obtaining precise results. Investigations have shown that by using the described microstructural approach by means of representative volume elements (RVE) the application of correct boundary conditions depends on the size of the volume element [38] such that above a certain element size, the numerical results of homogeneous and symmetric boundary conditions converge to an effective value, i.e. the result is not influenced by the choice of the boundary conditions anymore; but below that critical element size the results are influenced by the boundary conditions however.

In this study, the RVE size is usually above the critical element size. Therefore, the more straightforward homogeneous boundary conditions have been applied. Figure 14 shows that the bearings which represent in the ABAQUS model symmetry are assumed along the left side ($U_x = 0$) as well as the bottom side ($U_y = 0$). Due to the anisotropy of the plasma sprayed coating the loading direction is varied from the x-direction (perpendicular to the spraying direction) to the y-direction (in spraying direction), respectively. Depending on the loading direction either the right hand side of the structure is loaded in the x-direction ($U_x = 1$) or the top side is loaded in the y-direction ($U_y = 1$) while the other one is linked with the ABAQUS command *EQUATION to the displacement of the loaded side perpendicular to the loading direction. The origin point in the lower left corner is fixed ((0, 0); $U_x = 0$, $U_y = 0$).

Influence of the Threshold of Images on Mechanical Properties

Using the above detailed methodologies, the simulation provides the following results (Table 4). It is apparent, that porosity controls sensitively the mechanical behavior of such compound materials. When exceeding porosity values of some 15 %, the mechanical properties decrease significantly. With the increase of the brightness threshold, the computed effective elastic modulus decreases with a deceleration trend (Fig. 15 and Fig. 16).

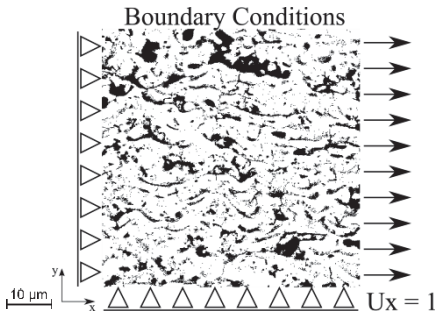

Figure 14: 2D problem (50 µm x 50 µm) definition with homogeneous boundary conditions. Symmetric boundary conditions on the bottom side and on the left side, respectively. Loading is applied on the right side in x-direction (displacement U in x-direction (arrows))

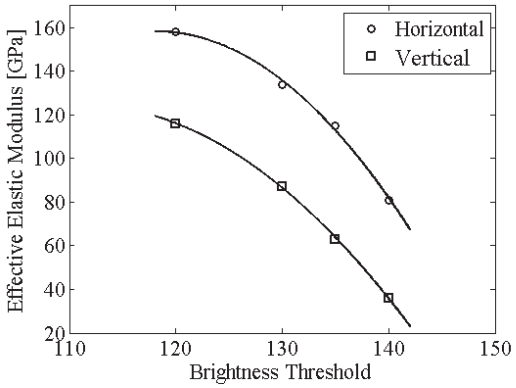

Figure 15: Relationship of the brightness threshold on the effective elastic modulus

Table 4: Porosity and the computed effective Elastic moduli E_{eff} vs. different thresholds of $MgAl_2O_4$

Threshold (/255)	Average Porosity	Effective elastic modulus [GPa]		$E_{eff,\parallel}$ / $E_{eff,\perp}$
		Horizontal	Vertical	
120	8.4%	158	116	1.4
130	12.0%	134	87	1.5
135	15.2%	115	63	1.8
140	19.6%	81	36	2.3

$E_{eff,\parallel}$ Elastic modulus parallel to the deposition surface (*horizontal*) and $E_{eff,\perp}$ Elastic modulus perpendicular to the deposition surface (*vertical*)

The elastic modulus differs significantly in the x- and y-directions. A value for the anisotropy of a plasma sprayed coating, which is used in literature [31], is the ratio of the effective modulus in the horizontal and vertical directions. Due to the increase of the difference in both directions, the ratio between the horizontal and vertical effective elastic moduli increases from 1.4 to 2.3 with increasing threshold (Table 4). The horizontal elastic modulus shows a good agreement with only 10 % deviation between simulation and experiment. With 4-point bending tests, an effective Young's modulus of 90 GPa was measured for the plasma sprayed $MgAl_2O_4$ coating. Comparing the simulation results to this experimentally determined value the horizontal modulus should be considered due to the loading conditions of the bending test perpendicular to the spraying direction. The average horizontal effective modulus of 81 GPa which was calculated with a threshold of 140 slightly underestimates the measured value of 90 GPa. The average porosity of 19.6% is reasonably close to the measured one of 21.1%, which confirms the found threshold.

Experimental data of the elastic modulus in the vertical direction is not yet available. However, McPherson et al. [39] describes the effective elastic modulus of a plasma-sprayed coating in the spraying direction (vertical) being in the range of one-fifth to one quarter of the bulk modulus. In this work, the numerically calculated vertical effective elastic modulus of 36 GPa is just slightly below one-fifth of the bulk modulus of 210 GPa.

With thresholds of 105 and 145 respectively for $MgAl_2O_4$ mixed with $SiC + Y_2O_3$ an effective horizontal modulus of 142 GPa and vertical of 93 GPa is calculated. This leads to a ratio of the effective modulus in the horizontal and vertical directions of 1.5. The porosity of this modelled microstructure achieves values of about 10.3%. This material shows the same ratio of the horizontal and vertical effective elastic values for the same porosity as the $MgAl_2O_4$ material.

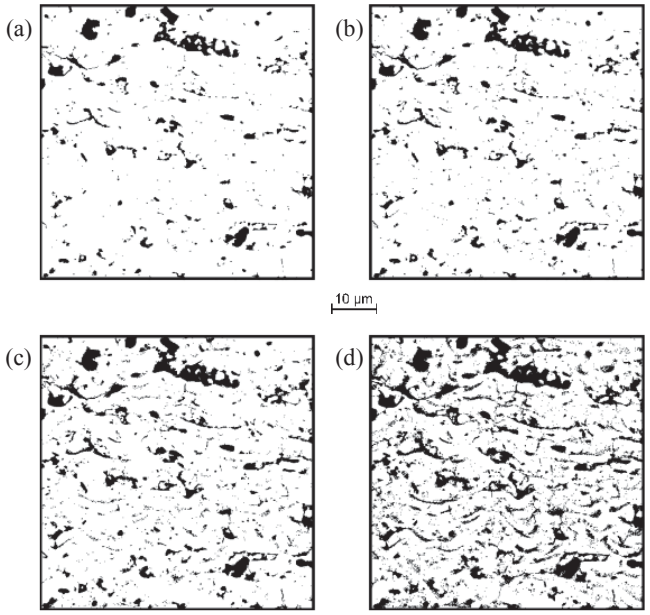

Figure 16: The same sections (50 µm x 50 µm) of the binary image obtained for different values of the threshold ((a) 120, (b) 130, (c) 135, (d) 140 from the SEM image (Fig. 10 (a))

Conclusions

Self-healing plasma sprayed $MgAl_2O_4$ coatings was investigated by incorporating $SiC+Y_2O_3$ as healing additives. It was observed that though SiC, even in nano sized particles, did not convert completely into SiO_2 after 10 hours of isothermal heat treatment at 1050°C. $SiC+Y_2O_3$ reacted after one hour to form a crystalline Y_2SiO_5 phase and most likely a vitreous $Y_2Si_2O_7$ phase. This is in spite of the fact that the reaction can only start after the onset of the oxidation of SiC. Hence though the healing reaction time could be decreased, reaction temperature remained above 1000°C. To lower the healing temperature a component would be needed to promote oxidation of SiC at lower temperatures. Moreover, in plasma sprayed spinel coatings with 20wt% ($SiC+Y_2O_3$) additive, the healing effect was inconclusive for less than 10 hours. Coating treated at 1050°C for 10 hours in air showed vitreous phase formation, closing of defects and coating consolidation. Mechanical properties data are being collected for healed coatings to evaluate improvement in the coating mechanical integrity. The developed self-healing coatings exhibited a CTE of 8.08 and 8.06 x 10^{-6} K^{-1} at 800°C before and after healing thermal treatment respectively. These values were marginally lower than that of pure spinel of 8.31 x 10^{-6} K^{-1}. Furthermore, the resistivity of the self-healing coating at high temperatures

remained comparable to spinel coatings. These CTE and resistivity values underlined applicability of the self-healing coatings as insulating ceramic deposits for high temperature fuel cells sealing.

For the image-based approach with the use of binary images of the $MgAl_2O_4$ material, it is observed that with a threshold of 140 a horizontal effective modulus of 81 GPa is found to be close to the measured value of 90 GPa. These findings are confirmed by comparing the calculated porosity value of 19.6% and measured porosity value of 21.1%, respectively, which is in good agreement with the experiment, too. The vertical effective elastic modulus amounts to 36 GPa which is approximately equal to one-fifth of the bulk modulus of 210 GPa, which is in good agreement with literature, too. Overall, the calculated effective elastic moduli in the vertical and horizontal directions, respectively, slightly underestimate the measured values.

The adapted image-based approach to determine the mechanical properties of the plasma-sprayed $MgAl_2O_4$ mixed with SiC + Y_2O_3, which possesses self-healing capabilities, is shown in this publication. The application on this new material required not only color separation of the SEM image with one threshold but also a second threshold for a further separation to take the self-healing phase into account.

Acknowledgement

This work was conducted with financial support of German Ministry of Education and Research (BMBF) for project "SHEACOAT" under grant no. WING-13X4012B. Contributions of Dr. Ruckdäschel with dilatometry and Dr. Hornauer for high temperature conductivity, as well as technical support from Mrs Plock, Mrs. Steinhilber, Mr. Roth and Mr. Thielke are acknowledged.

References

[1] J.J. Petrovic, L.A. Jacobson, "Controlled Surface Flaws in Hot-Pressed SiC", *J. Am. Ceram. Soc.*, 59 (1976) 34-37

[2] T.K. Gupta, "Crack Healing and Strengthening of Thermally Shocked Alumina", *J. Am. Ceram. Soc.*, 59 [5-6] (1976) 259-262.

[3] Z. Chlup, P. Flasar, A.Kotoji, I. Dlouhy, "Fracture Behaviour of Al_2O_3/SiC Nanocomposite Ceramics after Crack Healing Treatment", *J. Eur. Ceram. Soc.*, Vol. **28**, No. 5 (2008) pp. 1073-1077.

[4] K. Ando, K. Furusawa, K. Takahashi, M.C. Chu, S. Sato, "Crack-Healing Behavior of Structural Ceramics under Constant and Cyclic Stress at Elevated Temperature", *J. Ceram. Soc. Jpn.*, Vol. 110, No.8 (2002) pp. 741-747.

[5] M.C. Chu, S. Sato, Y. Kobayashi, K. Ando, "Damage Healing and Strengthening Behaviour in Intelligent Mullite/SiC Ceramics", *Fatigue Fract. Eng. Mater. Struct.*, Vol. 18, No. 9 (1995) pp. 1019-1029

[6] S.K. Lee, M. Ono, W. Nakao, K. Takahashi, K. Ando, "Crack-Healing Behaviour of Mullite/SiC/Y_2O_3 Composites and Its Application to the Structural Integrity of Machined Components", *J. Eur. Ceram. Soc.*, Vol. **25**, No. 15 (2005) pp. 3495-3502

[7] S.R. Choi, V. Tikare, "Crack Healing Behavior of Hot Pressed Silicon Nitride Due to Oxidation", *Scripta Metall. Mater.*, Vol. **26**, No. 8 (1992) pp. 1263-1268

[8] K. Ando, M.C. Chu, S. Matsushita, S. Sato, "Effect of Crack-Healing and Proof-Testing Procedures on Fatigue Strength and Reliability of Si_3N_4/SiC Composites", *J. Eur. Ceram. Soc.*, Vol. **23**, No. 6 (2003) pp. 977-984

[9] B.Y. Ma, J.K. Yu, Q. Zhu, Y. Sun, "Thermodynamic Analysis and Preparation of β-SiC/ZrO_2 Composites ", *Int. J. Min. Metall. Mater.*, Vol. **16**, No. 5 (2009) pp. 581-585

[10]K. Takahashi, Y.S. Jung, Y. Nagoshi, K. Ando, "Crack-Healing Behavior of Si_3N_4/SiC Composite under Stress and Low Oxygen Pressure", *Mater. Sci. Eng. A*, Vol. **527**, No. 15 (2010) pp. 3343-3345

[11]M. Kasiarova, J. Dusza, M. Hnatko, P. Sajgalik, "Microstructure and Fracture-Mechanical Properties of Carbon Derived Si_3N_4 + SiC Nanomaterials", *Mater. Sci. Eng. C*, Vol. **26**, No. 5-7 (2006) pp. 862-866

[12]S. Taniguchi, M. Kadowaki, T. Yasuo, Y. Akiyama, Y. Miyake and K. Nishio, "Improvement of Thermal Cycle Characteristics of a Planar-Type Solid Oxide Fuel Cell by Using Ceramic Fiber as Sealing Material", *J. Power Sources* Vol. **90**, No.2 (2000), pp. 163–169.

[13] C.-K. Lin, T.-T. Chen, Y.-P. Chyou, L.-K. Chiang, "Thermal Stress Analysis of a Planar SOFC Stack", *J. Power Sources*, Vol. **164**, No. 1 (2007) pp. 238-251

[14] J. Arnold, A. Ansar U. Maier, R. Henne, *International Thermal Spray Conference (ITSC),* (org.) German Welding Society (DVS), Maastricht, Netherlands 2008, CD-version

[15] F.L. Lowrie, R.D. Rawlings, "Room and High Temperature Failure Mechanisms in Solid Oxide Fuel Cell Electrolytes", *J. Eur. Ceram. Soc,.* Vol. **20**, No. 6(2000) 751–760.

[16] A. Ansar, G. Antou, and A. Denoirjean, *Proceedings of ITSC 2007,* (org.) ASM international, CD-version.

[17] A.A. Syed, Z. Ilhan, H. Weckmann, J. Arnold and G. Schiller, Improving Plasma Sprayed YSZ Coatings for SOFC Electrolytes, *J. Therm. Spray. Technol.*, 15(4) (2006) 617-622

[18] K. Shimoda, T. Koyanagi, Surface Properties and Dispersion Behaviors of SiC Nanopowders, *Colloids and Surfaces A: Physicochem. Eng. Aspects*, **463** (2014) 93–100

[19] J. Zhan, H. Wang, F. Zhu, S. Song. "Analysis on the Governing Reactions in Coal Oxidation at Temperatures up to 400˚C", *Inter. J. Clean Coal and Energy*, **3** (2014), 19-28

[20] Y. Kuroda, H. Hamano, T. Mori, Y. Yoshikawa, M. Nagao, "Specific Adsorption Behavior of Water on a Y_2O_3 Surface", *Langmuir*, Vol. 16, (2000), pp. 6937-

6947.
[21] R. Alfonsetti, L. Lozzi, M. Passacandanto, P. Picozzi, S. Santucci, "XPS Studies on SiO_x Thin Films", *Appl. Surf. Sci.*, Vol. 70/71, No. 1 (1993), pp. 222-225.
[22] S S. Contarini, S.P Howlett, C. Rizzo, B.A. de Angelis, "XPS Study on the Dispersion of Carbon Additives in Silicon Carbide Powders", *Appl. Surf. Sci.,* Vol. 51, No. 3-4 (1991), pp. 177-183.
[23] J. F. Moulder, W. F. Stickle, P. E. Sobol, and K. D. Bomben, Handbook of X-ray Photoelectron Spectroscopy, Perkin-Elmer Corporation (Eden Prairie, MN, 1992).
[24] M. Havel, Ph. Colomban, "Rayleigh and Raman Images of the Bulk/Surface Nanostructure of SiC Based Fibres", *Composites B*, 35 (2004) 139–147.
[25] Kazuya Shimoda, Takaaki Koyanagi, "Surface Properties and Dispersion Behaviors of SiC Nanopowders", *Colloids and Surfaces A: Physicochemical and Engineering Aspects*, 463 (2014) 93–100.
[26] Z. Wang, A. Kulkarni, S. Deshpande, T. Nakamura, H. Herman, "Effects of Pores and Interfaces on Effective Properties of Plasma Sprayed Zirconia Coatings", *Acta Materialia,* 2003*, 51*, 5319-5334
[27] Jiang-Hao Qiao, Rodolphe Bolot, H. Liao "Finite Element Modeling of the Elastic Modulus of Thermal Barrier Coatings", *Surface and Coatings Technology,* 2013*, 220*, 170-173
[28] Rodolphe Bolot, Jiang-Hao Qiao, Ghislaine Bertrand, Pierre Bertrand, Christian Coddet, "Effect of Thermal Treatment on the Effective Thermal Conductivity of YPSZ Coatings", Surface and Coatings Technology*,* 2013*, 220*, 170-173
[29] A. Zivelonghi, F. Cernuschi, C. Peyrega, D. Jeulin, S. Lindig, J. H. You, "Influence of the Dual-Scale Random Morphology on the Heat Conduction of Plasma-Sprayed Tungsten via Image-Based FEM", *Computational Materials Science,* 2013*, 68*, pp. 5-17
[30] GIMP 2.6, URL: http://www.gimp.org/ ; acc. 31.10.14
[31] P. Leßle, M. Dong, E. Soppa, S. Schmauder, "Simulation of Interpenetrating Microstructures by Self Consistent Matricity Models", *Scripta Mater*. 38, pp. 1327-1332 (1998).
[32] M. Dong, P. Leßle, U. Weber, S. Schmauder, "Mesomechanical Modelling of Composites Containing FGMs Related Interpenetrating Microstructures Based on Micromechanical Matricity Models", *Materials Science Forum* Vols. 308-311, pp. 1000-1005 (1999).
[33] CES Selector, Granta Design Ltd, Cambridge, UK
[34] Hyung-Jun Kim, Young-Gak Kweon, "Elastic Modulus of Plasma-Sprayed Coatings Determined by Indentation and Bend Tests", *Thin Solid Films*, 1999, 201-206
[35] OOF2, NIST, National Institute of Standards and Technology, URL: http://www.ctcms.nist.gov/oof/oof2/; acc.31.10.14
[36] ABAQUS 6.13 Manual
[37] Grasset-Bourdel, Renaud, « Structure/Property Relations of Magnesia-Spinel Refractories: Experimental Determination and Simulation », Université de Limoges, Science et Ingénierie en Matériaux, Mécanique, Energétique et Aéronautique (SI-MMEA)*,* 2011, PhD Thesis
[38] A. Ramazani, K. Mukherjee, U. Prahl, W. Bleck, "Modelling the Effect of Microstructural Banding on the Flow Curve Behaviour of Dual-Phase (DP) Steels", *Computational Materials Science*, 2012, 52, 46-54
[39] McPherson, R., "A Review of Microstructure and Properties of Plasma Sprayed Ceramic Coatings", *Surface and Coatings Technology*, 1989*, 39/40*, 173-181